Weyens, T., Sánchez, R., Huijsmans, G., Loarte, A., & García, L. (2017). PB3D: A new code for edge 3-D ideal linear peeling-ballooning stability. *Journal of Computational Physics*, 330, 997-1009.

DOI: https://doi.org/10.1016/j.jcp.2016.10.054

PB3D: A new code for edge 3-D ideal linear peeling-ballooning stability[☆]

T. Weyens[a,b,*], R. Sánchez[a], G. Huijsmans[b,d], A. Loarte[c], L. García[a]

[a] *Departamento de Física, Universidad Carlos III de Madrid, Madrid 28911, Spain*
[b] *Department of Applied Physics, Eindhoven University of Technology, PO Box 513, 5600 MB Eindhoven, Netherlands*
[c] *ITER Organization, Route de Vinon-sur-Verdon, CS 90 046, 13067 St. Paul Lez Durance Cedex, France*
[d] *Institute for Magnetic Fusion Research, CEA, 13108 Saint-Paul-lez-Durance, France*

Abstract

A new numerical code **PB3D** (**P**eeling-**B**allooning in **3**-**D**) is presented. It implements and solves the intermediate-to-high-n ideal linear magnetohydrodynamic stability theory extended to full edge 3-D magnetic toroidal configurations in previous work [1]. The features that make PB3D unique are the assumptions on the perturbation structure through intermediate-to-high mode numbers n in general 3-D configurations, while allowing for displacement of the plasma edge. This makes PB3D capable of very efficient calculations of the full 3-D stability for the output of multiple equilibrium codes. As first verification, it is checked that results from the stability code MISHKA [2], which considers axisymmetric equilibrium configurations, are accurately reproduced, and these are then successfully extended to 3-D configurations, through comparison with COBRA [3], as well as using checks on physical consistency. The non-intuitive 3-D results presented serve as a tentative first proof of the capabilities of the code.

Keywords: PB3D; ideal linear MHD stability; peeling-ballooning; high-n; edge; 3-D

1. Introduction

Magnetohydrodynamics (MHD) theory is a mathematically convenient and widely used tool in the study of hot plasmas, such as the ones appearing in toroidal magnetic

[☆] https://pb3d.github.io/

[*] Corresponding author: t.weyens@tue.nl

confinement devices, such as tokamaks and stellarators, even in regions in parameter space where, stricly speaking, the assumptions on which it is based are less valid. Nonetheless, MHD instabilities often lead to a rather hard limit on the stability of toroidal plasma configurations. Hence, it is important to study MHD in detail and the topic of interest in this work is the global ideal linear intermediate-to-high-n MHD stability of edge 3-D toroidal equilibrium configurations, where n is a measure of localization of the instabilities around the magnetic field lines.

The reason for focusing on the high-n assumption (also called "short-wavelength"), is that the resulting modes can be easily excited and can grow quickly, while at the same time spanning a large fraction of the plasma cross-section, which can give them the power to couple energy from the hot plasma core to the cold surface [6, sec. 7]. However, modes with more intermediate n numbers can also be important. The so-called *peeling-ballooning modes*, for example, are among the most important instabilities, where peeling modes have a distinct intermediate-n nature, whereas ballooning modes are described accurately through high-n theory. Among other things, they have been shown to be a prime candidate to explain the periodic outbursts observed experimentally, called ELMs [4], which can cause large power fluxes to the components in fusion devices and detoriate plasma confinement [5].

Here, the term intermediate-to-high-n therefore refers to an expansion in the parameter n accurate not just up to leading order in n, but also to second order. To preserve clarity, furthermore, in the remainder of this work, the term "high-n" is understood to include "intermediate-n" as well.

The high-n assumption was pioneered theoretically some time ago in the bulk plasma of axisymmetric configurations [7], after which it was extended to edge configurations [8], and also to bulk 3-D configurations [9]. An important common aspect of these theories, however, is that they all make use of Eikonal formulations for the spatial behavior (and normal modes for the time behavior) of the perturbation vector $\boldsymbol{\xi}(\mathbf{r}, t)$ of the form

$$\boldsymbol{\xi}(\mathbf{r}, t) = \boldsymbol{\xi}(\mathbf{r})\, e^{\mathrm{i}\omega t} = \hat{\boldsymbol{\xi}}(\mathbf{r})\, e^{\mathrm{i}nS(\mathbf{r})} e^{\mathrm{i}\omega t}\,, \tag{1}$$

where ω is the (complex) frequency of the normal mode and S is the Eikonal, defined

through

$$\mathbf{B} \cdot \nabla S = 0 \,, \tag{2}$$

with $\mathbf{B}$ the magnetic field, which through the large factor n decouples the derivatives into a slow derivative parallel to the magnetic field and a fast derivative perpendicular to it. Subsequently, through judicious choices of the form and behavior of the amplitude $\hat{\boldsymbol{\xi}}$, this carries on to decoupling of the MHD equations in different orders. Finally, the lowest order is then decoupled for the flux surfaces, and yields an ordinary differential equation[1], usually known as the *ballooning equation*, that describes the stability for every flux surface separately. Higher orders typically yield the shape of the amplitude function $\hat{\boldsymbol{\xi}}$.

For a full description of a general high-n mode, however, an Eikonal cannot be used easily, as it suffers from important limitations, such as the lack of periodicity [10] which makes it difficult to reconstruct periodic solutions, the assumed shapes for the perturbation amplitudes, and the difficulty of treating the cases in which the edge of the plasma is perturbed.

Because of these reasons, as an alternative, general Fourier modes of the form $\sim \hat{\boldsymbol{\xi}}(\psi) \exp[n\zeta - m\theta]$ can be used instead in a (ψ, θ, ζ) coordinate system with ψ a flux coordinate and θ poloidal and ζ toroidal angles. A flux coordinate is a function that monotomously varies accross the nested flux surfaces of ideal plasmas (i.e. without resistivity), such as enclosed volume or flux; and it is convenient to deform the angular coordinates so that the magnetic field becomes straight [11]. Furthermore, the correct treatment of edge-perturbed plasmas is also possible, through formally considering the toroidal system as the union of the plasma and a surrounding vacuum, connected by an edge that in theory can support a jump in the magnetic field through a skin current, and by investigating the perturbed potential and kinetic energy of the whole system; a strategy refered to as the *extended energy principle* [12].

For axisymmetric equilibria, this was the approach followed by the numerical code ELITE [4]. In PB3D the approach is more general, as full 3-D configurations are

[1] Or possibly a set of two if the plasma is compressible. [9]

considered, and when they are restricted to axisymmetry, this leads to the same range of validity as the original ELITE[2]. In 3-D, one would expect greater complexity and computational requirements, but an important finding of the theory behind PB3D [1], is that the numerical problem to be solved is not substantially more complex than that for the axisymmetric case, as the fluted (see subsec. 2.2) high-n nature of the modes leads naturally to a separation of scales that reduces the dimension of the problem by one.

Apart from this, to motivate the search for a 3-D solution, some examples of 3-D configurations include the breaking of axisymmetry, such as due to the usage of ferromagnetic Tritium Breeder Modules in ITER, discrete toroidal field coils in tokamaks that introduce a toroidal field ripple, or axisymmetry-breaking resonance magnetic perturbation (RMP) coils for ELM control that work by explicitely breaking axisymmetry. Recently, these topics have started attracting ample interest, and mostly so for the RMP coils, as ELM control is becoming very important in the next-generation tokamaks such as ITER.

In [13], for example, the 3-D corrugation of the plasma edge was identified as one of the key ingredients in the mechanism of ELM control through RMPs, (the simulation of which is a task for which PB3D would be very well suited). As an alternative to full 3-D treatments, perturbative approaches to 3-D effects were used in both [14] and [15], where the former is geared mostly towards configurations with magnetic islands, and the latter towards 3-D modifications of otherwise axisymmetric equilibria. Finally, work with the CAS3D code that is able to perform 3-D stability analysis, but which does not employ the high-n assumption, was presented already in [16]. That research was geared towards stellarators, which are fully 3-D configurations, that can also suffer from instability issues, and where perturbative approaches are not possible.

After this introduction to and situation of the current work, the theoretical model derived in [1] is shortly summarized in the next section. Subsequently, in sec. 3, numerical aspects of the new PB3D code, such as the discretization methods and employed algorithms, are discussed. Following this, in sec. 4 information is given about

[2]ELITE has recently been extended to include a higher order in the expansion in n, not yet present in the PB3D theory.

the verification of PB3D, making use of comparisons with numerical codes MISHKA [2] and COBRA [3], as well as checks on physical consistency. Finally, in sec. 5, a summary follows.

2. Theoretical model

The theoretical model on which the PB3D code is based, was developed in [1] and is shortly summarized here. First, some general information is given about the extended energy principle that is used and afterwards the description of the magnetic field is discussed, as well as the specific form of the perturbations used in this work. Finally, stability is investigated, making use of minimized energy.

2.1. Extended energy principle

As discussed in the previous section, the extended principle is used for normal modes with frequency ω. This leads to expressions for the perturbed potential and kinetic energy for the system composed of plasma connected to surrounding vacuum at the plasma edge. It is advantageous to make use of the *Rayleigh Quotient* formulation which identifies eigenvalues ω^2 of the normal modes with stationary values of the quotient Λ, defined as the ratio of perturbed potential and kinetic energy:

$$\Lambda\left[\boldsymbol{\xi}, \mathbf{Q}_\mathrm{v}\right] \equiv \frac{\delta W\left[\boldsymbol{\xi}, \mathbf{Q}_\mathrm{v}\right]}{K\left[\boldsymbol{\xi}\right]} \equiv \frac{\delta W_\mathrm{p}\left[\boldsymbol{\xi}\right] + \delta W_\mathrm{s}\left[\boldsymbol{\xi}\right] + \delta W_\mathrm{v}\left[\mathbf{Q}_\mathrm{v}\right]}{\frac{1}{2}\int_\mathrm{p} \rho \left|\boldsymbol{\xi}\right|^2 \mathrm{d}\mathbf{r}} \,, \tag{3}$$

where ρ is the plasma mass density and $\boldsymbol{\xi}$ and $\mathbf{Q}_\mathrm{v}$ are the plasma, respectively the vacuum magnetic field perturbation, and where it is illustrated that the perturbed potential energy is composed of parts corresponding to the plasma (subscript p), the edge surface (s) and the surrounding vacuum (v):

$$\begin{cases} \delta W_\mathrm{p}\left(\boldsymbol{\xi}\right) = \dfrac{1}{2}\displaystyle\int_\mathrm{p} \mathrm{d}\mathbf{r} \left[\frac{\left|\mathbf{Q}\right|^2}{\mu_0} - \xi^* \cdot \mathbf{J} \times \mathbf{Q} + \gamma p \left|\nabla \cdot \xi\right|^2 + \left(\xi \cdot \nabla p\right) \nabla \cdot \xi^*\right] \\ \delta W_\mathrm{s}\left(\boldsymbol{\xi}\right) = \dfrac{1}{2}\displaystyle\int_\mathrm{s} \mathrm{d}S \left[\left|\mathbf{n} \cdot \boldsymbol{\xi}\right|^2 \mathbf{n} \cdot \left[\!\left[\nabla\left(\mu_0 p + \frac{B^2}{2}\right)\right]\!\right]\right]_\mathrm{s} \\ \delta W_\mathrm{v}\left(\mathbf{Q}_\mathrm{v}\right) = \dfrac{1}{2}\displaystyle\int_\mathrm{v} \mathrm{d}\mathbf{r} \left[\frac{\left|\mathbf{Q}_\mathrm{v}\right|^2}{\mu_0}\right] . \end{cases} \tag{4}$$

Here, $\mathbf{J}$ is the plasma current, defined through $\mu_0\mathbf{J} = \nabla \times \mathbf{B}$, p is the plasma pressure, γ the adiabatic constant, $\mathbf{n}$ the unit vector normal to the plasma edge surface and the quantity $\mathbf{Q}$ is the perturbation of the magnetic field

$$\mathbf{Q} = \nabla \times (\boldsymbol{\xi} \times \mathbf{B}) \ . \tag{5}$$

An advantage of the generalized energy principle, is that the perturbations only need to satisfy the *essential boundary conditions*

$$\begin{cases} \boldsymbol{\xi} \text{ regular} & \text{(on p)} \ , \\ \mathbf{n} \cdot \nabla \times (\boldsymbol{\xi} \times \mathbf{B}_\mathrm{v}) = \mathbf{n} \cdot \mathbf{Q}_\mathrm{v} & \text{(on s)} \ , \\ \mathbf{n} \cdot \mathbf{Q}_\mathrm{v} = 0 & \text{(on exterior wall)} \ , \end{cases} \tag{6}$$

as the natural boundary conditions are already taken into account automatically.

2.2. Magnetic field and Fourier modes

Fourier modes are used in the angular coordinates θ and ζ, which in this work are chosen so that the magnetic field

$$\mathbf{B} = \nabla\zeta \times \nabla\psi + q(\psi)\nabla\psi \times \nabla\theta \ , \tag{7}$$

appears straight with its pitch constant on each flux surface and given by the *safety factor* $q\,(\psi) = \frac{\mathrm{d}\zeta}{\mathrm{d}\theta}$, with as flux coordinate the scaled enclosed poloidal flux $\psi = \frac{\psi_\mathrm{pol}}{2\pi}$. To further simplify the situation, the toroidal coordinate, is replaced by the *field line label* $\alpha = \zeta - q\theta$, the resulting magnetic field being proportional to the covariant unit vector in the θ direction:

$$\mathbf{B} = \frac{1}{\mathcal{J}}\mathbf{e}_\theta \ , \tag{8}$$

with $\mathcal{J}$ the Jacobian, which is why θ is called the *parallel coordinate* or *magnetic coordinate*.[3] In the resulting (α, ψ, θ) coordinate system, the Fourier modes then have the form:

$$\boldsymbol{\xi}\,(\alpha, \psi, \theta) = \hat{\boldsymbol{\xi}}\,(\psi)\, e^{\mathrm{i}\left[(nq-m)\theta - n\alpha\right]} \ . \tag{9}$$

[3]This is the for the case when the enclosed poloidal flux is used as normal coordinate. If the toroidal flux is used, the parallel coordinate is not θ but ζ. PB3D is capable of this, but the rest of the discussion is limited to using the poloidal flux as normal coordinate.

From basic stability considerations, it can be seen that acceptable high-n modes must be *fluted* [17, sec. 8.11], meaning that their parallel dependence should be of the same order as the equilibrium variations, as opposed to their fast perpendicular dependence. The introduction of the α coordinate then leads to a natural separation of these two length scales that decouples the modes that belong to different field lines as is illustrated in [1, fig. 1]. This is expressed in the exponent of eq. 9 through the condition $\frac{nq-m}{n} \ll 1$.

2.3. Minimized perturbed energy

Employing the Fourier form of the perturbations of eq. 9 in the expressions for the perturbed energies of eqs. 4, through the analytical minimization of certain stabilizing term the different components of the perturbation can all be written in terms of the normal component $X = \nabla\psi \cdot \boldsymbol{\xi}$, and through the decoupling of modes belonging to different field lines, the mode vector of the perturbation, $\mathbf{X} = (X_1, X_2, \ldots, X_M)^T$ contains only M components due to the θ dimension. The resulting expressions for the perturbed plasma potential and kinetic potential then reduce to integrals over ψ of bilinear form relating the vector of the modes of $\boldsymbol{\xi}$ to the perturbed energies:

$$\delta W_\mathrm{p} = \frac{1}{2}\int_\mathrm{v} \mathbf{X}^* \overline{\mathbf{P}} \mathbf{X}\, \mathrm{d}\psi \,, \tag{10}$$

$$K = \frac{1}{2}\int_\mathrm{v} \mathbf{X}^* \overline{\mathbf{K}} \mathbf{X}\, \mathrm{d}\psi \,, \tag{11}$$

where the tensors $\overline{\mathbf{P}}$ and $\overline{\mathbf{K}}$ are both of the same form, so they can be bundled by defining the Lagrangian

$$\overline{\mathbf{L}} = \overline{\mathbf{P}} - \omega^2 \overline{\mathbf{K}} \,, \tag{12}$$

with elements $\overline{L}_{k,m}$ given by, using non-standard terminology, *magnetic average modes* of the quantities $L_{k,m}$, defined as

$$\overline{L}_{k,m} = \int_\alpha \mathcal{J} e^{\mathrm{i}(k-m)\theta} L_{k,m}\, \mathrm{d}\theta \,, \tag{13}$$

where the integration runs along a field line with label α. Note that this is a consequence of the fact that only modes pertaining to the same field lines are coupled. Also note that the Lagrangian formulation is equivalent to using the Rayleigh Quotient.

The quantities $L_{k,m} = P_{k,m} - \omega^2 K_{k,m}$ are second order differential operators with elements of the form

$$L_{k,m} = L^0_{k,m} + \frac{\overleftarrow{\mathrm{d}}}{\mathrm{d}\psi} L^{1*}_{m,k} + L^1_{k,m} \frac{\overrightarrow{\mathrm{d}}}{\mathrm{d}\psi} + \frac{\overleftarrow{\mathrm{d}}}{\mathrm{d}\psi} L^2_{k,m} \frac{\overrightarrow{\mathrm{d}}}{\mathrm{d}\psi} \,, \tag{14}$$

which are Hermitian, since $L^0_{k,m}$ and $L^2_{k,m}$ are individually so. This expresses the fact that there are no losses in ideal MHD. The arrows in above equation indicate the direction in which the derivatives are to be taken.

Apart from this, the perturbed energy of the vacuum reduces to a surface term $\delta^{\mathrm{vac}}_{k,m}$, and it can be shown that a perturbed skin current on the plasma edge is not allowed as it would be very stabilizing, so that the contribution due to the edge is zero.

Finally, Euler minimization of the Rayleigh Quotient in the different functions $X^*_k(\psi)$ leads to a coupled set of second-order ordinary differential equations (ODEs) of the functions $X_m(\psi)$ that contain an eigenvalue ω^2 due to the time derivatives present in the kinetic energy as related to the square of the velocity. Furthermore, the necessary partial integrations that translate normal derivatives of the complex conjugate functions X^*_k, introduce boundary terms at the edges of the integration boundaries in ψ, which leads to a contribution at the plasma edge, which is added to the contribution $\delta^{\mathrm{vac}}_{k,m}$ due to the vacuum—the contribution at the plasma center vanishes as the perturbations are assumed to vanish there; core instabilities are not the interest of high-n theory.

Therefore, the resulting system of equations is of the form

$$\sum_m \left\{ \overline{L}^0_{k,m} X_m - \left(\overline{L}^{1*}_{m,k} X_m \right)' + \overline{L}^1_{k,m} X'_m - \left(\overline{L}^2_{k,m} X'_m \right)' \right\} = 0 \,, \tag{15}$$

and a total surface contribution

$$\sum_m \left\{ \left(\delta^{\mathrm{vac}}_{k,m} + \overline{L}^{1*}_{m,k} \right) X_m + \overline{L}^2_{k,m} X'_m \right\} = 0 \,, \tag{16}$$

with the primes indicating normal derivatives. With $k = 1 \ldots M$ and $m = 1 \ldots M$, these are M equations for M functions X_m, containing an eigenvalue ω^2, and the second equation serves as a boundary condition for the first, combined with the boundary condition of vanishing perturbations at the plasma center, mentioned earlier.

Expressions for the elements of the tensors $P^j_{k,m}$, pertaining to the plasma potential

energy δW_{p}, and $K^j_{k,m}$, to the plasma kinetic energy K are given for $j = 0 \ldots 2$ by:

$$\begin{cases} P^0_{k,m} = \dfrac{1}{\mu_0}\dfrac{|\nabla\psi|^2}{\mathcal{J}^2 B^2}\left(DU^{0*}_k - \mathcal{J}S - \mu_0\sigma\dfrac{\mathcal{J}B^2}{|\nabla\psi|^2}\right)\left(DU^0_m - \mathcal{J}S - \mu_0\sigma\dfrac{\mathcal{J}B^2}{|\nabla\psi|^2}\right) \\ \qquad\qquad - \dfrac{\sigma}{\mathcal{J}}\left(\mathcal{J}S + \mu_0\sigma\dfrac{\mathcal{J}B^2}{|\nabla\psi|^2}\right) + \dfrac{(nq-k)\,(nq-m)}{\mu_0\mathcal{J}^2\,|\nabla\psi|^2} - 2p'\kappa_n \\ P^1_{k,m} = \dfrac{1}{\mu_0}\dfrac{|\nabla\psi|^2}{\mathcal{J}^2 B^2}\left(DU^{0*}_k - \mathcal{J}S - \mu_0\sigma\dfrac{\mathcal{J}B^2}{|\nabla\psi|^2}\right)DU^1_m \\ P^2_{k,m} = \dfrac{1}{\mu_0}\dfrac{|\nabla\psi|^2}{\mathcal{J}^2 B^2}DU^1_m DU^{1*}_k\ . \end{cases} \tag{17}$$

and

$$\begin{cases} K^0_{k,m} = \dfrac{\rho}{|\nabla\psi|^2} + \dfrac{|\nabla\psi|^2}{B^2}U^{0*}_k U^0_m\rho \\ K^1_{k,m} = \dfrac{|\nabla\psi|^2}{B^2}U^{0*}_k U^1_m\rho \\ K^2_{k,m} = \dfrac{|\nabla\psi|^2}{B^2}U^{1*}_k U^1_m\rho\ , \end{cases} \tag{18}$$

where S is the shear, σ is the parallel current and κ_n and κ_g are the normal and geodesic components of the curvature:

$$S = -\frac{1}{\mathcal{J}}\frac{\partial\Theta^\alpha}{\partial\theta}\ , \tag{19}$$

$$\sigma = \frac{\epsilon_{ijk}}{\mu_0}\frac{1}{B^2\mathcal{J}}\frac{\partial B_j}{\partial u^i}B_k\ , \tag{20}$$

$$\kappa_n = \frac{\nabla\psi}{|\nabla\psi|^2\,B^2}\cdot\nabla_\perp\left(\mu_0 p + \frac{B^2}{2}\right)\ , \tag{21}$$

$$\kappa_g = -\frac{1}{2p'}\frac{1}{\mathcal{J}}\frac{\partial\sigma}{\partial\theta}\ , \tag{22}$$

making use of the covariant components of the magnetic field $B_i = g_{\theta,i}/\mathcal{J}$ and the following definition for Θ^i:

$$\Theta^i = \frac{\nabla\psi\cdot\nabla u^i}{\nabla\psi\cdot\nabla\psi}\ . \tag{23}$$

Subsequently, the quantities U^i_m and DU^i_m, for $i = 0, 1$, correspond to the geodesic component of the plasma perturbation $U = \frac{\nabla\psi\times\mathbf{B}}{|\nabla\psi|^2}\cdot\boldsymbol{\xi}$, minimized as a function of the normal component X, and the parallel derivative:

$$U_m = \left[U^0_m + U^1_m\frac{\mathrm{d}}{\mathrm{d}\psi}\right](X_m)\ , \tag{24}$$

$$DU^i_m = \frac{\partial U^i_m}{\partial\theta} + \mathrm{i}\,(nq-m)\,U^i_m\ , \tag{25}$$

where

$$\begin{cases} U_m^0 = -\left(\Theta^\alpha + q'\theta\right) + \dfrac{\mathrm{i}}{n}\dfrac{1}{B_\theta}\left[B_\alpha q' + \mathcal{J}\mu_0 p' + \mathrm{i}\left(nq - m\right)\left(B_\alpha q'\theta - B_\psi\right)\right] \\ \qquad + \dfrac{\mathrm{i}}{n}\dfrac{1}{B_\theta}\dfrac{nq-m}{n}\mathcal{J}\mathbf{B}\cdot\nabla\psi\times\nabla\left(\Theta^\theta e^{\mathrm{i}(nq-m)\theta}\right)e^{-\mathrm{i}(nq-m)\theta}\,, \\ U_m^1 = \dfrac{\mathrm{i}}{n}\left(1 + \dfrac{nq-m}{n}\dfrac{B_\alpha}{B_\theta}\right)\,. \end{cases} \tag{26}$$

and the remaining quantities have their usual meaning.

A discussion concerning the physical meaning of the different terms in above equations is given in [1].

3. Numerical aspects of PB3D

In this section, first the discretization of the system of ODEs is discussed, followed by a subsection considering the code structure and a section giving information about the used algorithms.

3.1. Discretization

In PB3D, functions $X_m(\psi)$ are discretized using finite differences at I normal positions ψ_i. The M different modes are then bundled at each of these I normal positions into the new vector $\mathbf{X}$ of size $I \times M$ whose components $X_{mi} \equiv X_m(\psi_i)\, e^{-\mathrm{i}m\theta}$.

Subsequently discretizing the differential operators of eqs. 15 and 16 then naturally leads to a generalized eigenvalue problem of the form:

$$\mathbf{AX} = \lambda\mathbf{BX}\,, \tag{27}$$

with $\mathbf{A}$ and $\mathbf{B}$ matrices corresponding to the potential and kinetic energy, $\mathbf{X}$ the eigenvector and $\lambda = \omega^2$ the eigenvalue, so that $\lambda > 0$ denotes stability and $\lambda < 0$ instability. The discretized boundary condition (eq. 16) enters in the last rows and columns of the matrices and the other boundary condition, the vanishing of the discretization at the plasma center, at the first rows and columns.

Importantly, if the discretization is done judiciously, $\mathbf{A}$ and $\mathbf{B}$ are Hermitian, reflecting the energy-conserving nature of ideal MHD in a numerical way. Though PB3D

can handle this process using central differences of arbitrary order, for the sake of illustration, only the results for the first order are described here, using

$$\begin{aligned} f^{(1)} &= \frac{f_{i+1} - f_{i-1}}{\Delta} - \frac{\Delta^2}{6} f^{(3)} + O\left(\Delta^4\right) \\ &\approx \frac{f_{i+1} - f_{i-1}}{\Delta} \,, \end{aligned} \tag{28}$$

with constant step size $\Delta = \psi_{i+1} - \psi_i$. Defining the discretized Lagrangian as $\mathbf{L} \equiv \mathbf{A} - \lambda \mathbf{B}$, the generalized eigenvalue equation becomes

$$\mathbf{L}\mathbf{X} = 0 \,, \tag{29}$$

where now the bar notation is left out as henceforth all the quantities are assumed to be magnetic average modes.

Discretizing the Euler eq. 15, the bulk of the matrix $\mathbf{L}$ is found to be given by the superposition along the diagonal of a Hermitian *stencil* consisting of nine $(M \times M)$ blocks of the form

$$\begin{pmatrix} \left(\frac{1}{2\Delta}\right)^2 \mathbf{L}_i^2 & -\frac{1}{2\Delta}\mathbf{L}_i^{1\dagger} & -\left(\frac{1}{2\Delta}\right)^2 \mathbf{L}_i^2 \\ -\frac{1}{2\Delta}\mathbf{L}_i^1 & \mathbf{L}_i^0 & \frac{1}{2\Delta}\mathbf{L}_i^1 \\ -\left(\frac{1}{2\Delta}\right)^2 \mathbf{L}_i^2 & \frac{1}{2\Delta}\mathbf{L}_i^{1\dagger} & \left(\frac{1}{2\Delta}\right)^2 \mathbf{L}_i^2 \end{pmatrix} \,. \tag{30}$$

The matrix $\mathbf{L}$ is adapted at the first and last normal position $i = 1$ and $i = I$ to incorporate the boundary conditions. At the first position, the perturbation is set to zero by introducing an artificial eigenvalue λ_{BC} and adapting the first row and column block of the matrices $\mathbf{A}$ and $\mathbf{B}$ to

$$\mathbf{A}_{ij} = \begin{cases} \mathbb{1}\lambda_{\mathrm{BC}} & \text{if} \quad i = j = 1 \\ 0 & \text{if} \qquad \text{else} \end{cases} \quad \text{and} \quad \mathbf{B}_{ij} = \begin{cases} \mathbb{1} & \text{if} \quad i = j = 1 \\ 0 & \text{if} \qquad \text{else} \end{cases} \,. \tag{31}$$

The stencil at the last position $i = I$ is modified using the boundary condition from eq. 16

$$\begin{pmatrix} 0 & \frac{1}{2\Delta}\boldsymbol{\delta}^{\mathrm{vac}} & 0 \\ \frac{1}{2\Delta}\boldsymbol{\delta}^{\mathrm{vac}} & \mathbf{L}_I^{0,\mathrm{mod}} & 0 \\ 0 & 0 & 0 \end{pmatrix} \,, \tag{32}$$

with

$$\mathbf{L}_I^{0,\mathrm{mod}} = \mathbf{L}_I^0 - \left(\mathbf{L}_I^1 + \boldsymbol{\delta}^{\mathrm{vac}}\right)\left(\mathbf{L}_I^2\right)^{-1}\left(\mathbf{L}_I^1 + \boldsymbol{\delta}^{\mathrm{vac}}\right)^{\dagger} \,. \tag{33}$$

Finally, it is interesting to note that the stencil from eq. 30, which resulted from the discretization of the Euler equation (eq. 15), can also be interpreted directly as the terms in the Lagrangian by considering the quadratic form $\frac{1}{2}\mathbf{X}^\dagger\mathbf{L}\mathbf{X}$ as the discretized version of

$$\mathcal{L} = \delta W - K = \frac{1}{2}\int_{\mathrm{V}} \mathbf{X}^* \left(\overline{\mathbf{P}} - \omega^2 \overline{\mathbf{V}}\right)\mathbf{X}\,\mathrm{d}\psi\ , \tag{34}$$

the discretized integral reduced to a summation in the quadratic form. Indeed, the factors of the stencil that builds up $\mathbf{L}$ have a clear connection to the terms of the operators $\mathbf{V}^j$ and $\mathbf{K}^j$ in eq. 14, the terms for $j = 0$ ending up in the central elements of the stencil, the terms with $j = 1$ in the main row and column and the terms with $j = 2$ in the diagonal elements. As a consequence, it can be seen that an extension to higher orders central differences is straightforward: The stencil of eq. 30 then just grows in size and the factors change. Practially, apart from an easy way to implement general discretization orders, this is of importance as well as it can be seen that explicit storage of (only the nonzero elements of) the matrix will contain a lot of redundant information. It is then better to make use of so-called *matrix-free methods*, where only the operations of the matrix on vectors or matrices are defined in the numerical code.

3.2. Code structure

PB3D is written in a modular way, so that it can be run using the output of various equilibrium codes and to make the stability calculation customizable.

The essence of PB3D consists of four major parts called drivers: the *input driver*, the *equilibrium driver*, the *perturbation driver* and the *solution driver*. There is also a standalone program called POST that does the post-processing of PB3D output, with a single driver. The different drivers function completely independently, to allow for easy modularization, with communication between them going exclusively through optimized HDF5 channels using an output data file, for the large datasets, as well as some minor global variables for book-keeping. Apart from this, PB3D makes use of the technique of *Richardson extrapolation* [18, sec. 16.4] as well as methods of keeping the memory usage below a threshold, on three different levels. Finally, the whole PB3D code is parallelized using MPI to make efficient use of modern computing resources. Figure 1 explains this general structure.

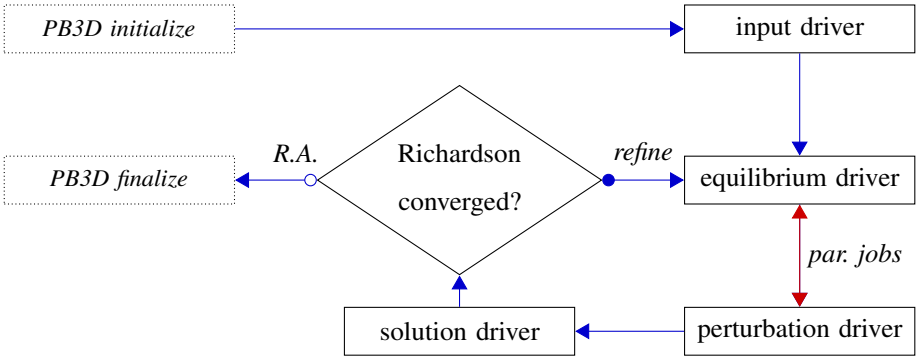

Figure 1: PB3D general flowchart. In every Richardson level, it is checked whether the relative error between successive levels falls below a threshold. If not, the parallel grid is *refined*; If so, Richardson extrapolation (*R.A.*) is applied to get an approximation of higher precision. An explanation for the double arrow labeled *par. jobs* is given below, in the paragraph concerning the equilibrium driver. PB3D outputs the relevant variables using HDF5 at completion of each driver, and reads them in the subsequent drivers, but this is not portrayed here.

Note that to find the straight field line coordinates, a similar procedure is done as in [3], i.e. by finding the zero's of

$$\alpha - \zeta + q\theta = 0 \,, \tag{35}$$

but here a variant of Brent's algorithm, called Zhang's algorithm [19], is used.

Subsequently, a word should be said about the ways in which PB3D treats the perturbation mode numbers. One can either choose between prescribing them manually, setting a primary mode number n (fast-varying field line label α; no coupling) and the secondary mode number m (slowly-varying parallel coordinate θ; coupling). However, it is usually more efficient to use the *fast version*, where the user prescribes only the number of secondary modes numbers. PB3D will then automatically calculate the mode numbers that are closest to resonance $nq \approx m$. Not only does this greatly reduce the number of modes, and thus the computing time necessary, but it will also result in matrices **A** and **B** that are much better conditioned as the whole theory behind PB3D is built on this resonant condition.

Finally, in the next paragraphs, some more information is given about the method of

richardson extrapolation, as well as on so-called *energy reconstruction*.

Richardson Extrapolation. Richardson extrapolation is used in PB3D to get better approximations to the numerical integrals of the field lines averages. Use is made of explicit knowledge of the discretization scheme, so that the results for numerical grids with equal boundaries but different numbers of points are combined to reduce the error further. More exactly, for equidistant step size $\Delta\psi$ and discretization through finite differences of order 1, the difference between the true mathematical operator in eq. 15 and the discretized version is indicated by the operator

$$\delta\overline{L}\left[X\right] = \sum_{l=1}^{\infty} \frac{\Delta\psi^{2l}}{(2l+1)!} \left[\overline{L}^{1} X^{(2l+1)} - \left(\overline{L}^{1^{\dagger}} X\right)^{(2l+1)} - \sum_{j=0}^{\infty} \frac{\Delta\psi^{2j}}{(2j+1)!} \left(\overline{L}^{2} X^{(2j+1)}\right)^{(2l+1)} \right] , \tag{36}$$

where the superscripts indicate normal derivatives. For general discretizaion orders p, this can be written as

$$\delta\overline{L} = \sum_{l=1}^{\infty} a_l \Delta\psi^{2pl} \, . \tag{37}$$

Assuming the same kind of dependence on the resulting eigenvalue as well, the information from the solutions of R of different step sizes can be combined, yielding a recursive formula for $\lambda_r^{(R)}$ [20, p. 270]

$$\lambda_r^{(R)} = \lambda_{r-1}^{(R)} + \frac{\lambda_{r-1}^{(R)} - \lambda_{r-1}^{(R-1)}}{2^{2pr} - 1} \quad \text{for } r = 1 \ldots R \, , \tag{38}$$

with $\lambda_0^{(R)}$ the eigenvalue. This expression is then an approximation of order $O\left(\Delta\psi^{2p(R+1)-1}\right)$ to the physical eigenvalue.

The fact that the parallel grids used in PB3D are equidistant, with the set of points of a certain Richardson level r equal to the set of points of the previous level $r-1$, *plus* the set of intermediary points, has implications. An important advantage is that for Newton-Cotes formulas of order 1 and 3 (i.e. trapezoidal rule and Simpson's 3/8 rule), not only the *points* but the entire *integrals* calculated for the previous Richardson levels can be used in the calculation of the integrals of the current level, which cuts memory usage almost by half. For these Newton-Cotes rules, the integral I_r calculated with all the points of a Richardson level $r > 1$ is given by:

$$I_r = \frac{I_{r-1}}{2} + K_r \, , \tag{39}$$

where K_r is a combination of only the new points for this Richardson level (i.e. the intermediary points with respect to the points of level $r - 1$), differing slightly from the general Newton-Cotes formulas to account for boundary effects.[4]

As explained in fig. 1, after each Richardson level $r > 1$, PB3D checks whether the relative difference between the eigenvalue found in this level and the previous level is lower than a certain threshold. If so, Richardson extrapolation is applied to combine the eigenvalues calculated for all the previous levels $1 \dots r$ into the approximation with the lowest error. If convergence is not yet reached, the process starts again after refining the parallel grid by adding the intermediate points, as stated above. Again, it should be noted that the calculations for the next Richardson level will then only use these intermediary points, i.e. half the refined grid, which is not a general feature of Richardson extrapolation schemes. Note that, as the eigenvectors are a function of the normal coordinate only, the eigenvectors found for the current Richardson level can be used easily as a first guess for the next one, sometimes drastically cutting computing time.

Finally, the modular structure of PB3D grants the opportunity for restart. A simulation that has been done up to Richardson level r can be (re)started up to level $r + 1$. This allows for added control of the Richardson extrapolation loop.

Energy reconstruction. POST is a complementary post-processing program for PB3D output. Among other things, it is worth mentioning that in POST *energy reconstruction* is performed, by which the following is meant: The eigenvector can be used to calculate the individual terms that constitute the plasma potential as well as kinetic energy. Not only does this provide a final and thorough check on consistency[5] through checking whether the Rayleigh Quotient Λ from eq. 3 is equal to the eigenvalue λ, it also allows for the individual inspection of these terms to ascertain their individual strenghts, for

[4]For example, for Simpson's 3/8 rule, the coefficients of quadrature c_i in $\int f(\psi)\,\mathrm{d}\psi \approx \frac{3}{8}\Delta\psi \sum_i c_i f_i = I_r$ are given by 1 3 3 2 3 3 2 $\cdots$ 2 3 3 1, and have to be modified to 3 3 2 3 2 $\cdots$ 2 3 3 for K_r.

[5]Naturally, these terms do end up in the matrices **A** and **B** of the generalized eigenvalue equation (eq. 27) through the vectorial and tensorial perturbation variables discussed in the previous paragraphs, but only after algebraic manipulations that do not preserve their individuality.

example to see whether an instability is current- or pressure-driven.

4. Verification

The PB3D is verified by comparing it with other numerical codes, as well as using criteria of physical consistency. In a first subsection, the axisymmetric equilibrium model CBM18 is discussed, which is then used in subsec. 4.2 to perform verification for axisymmetric configurations. Subsequently, this is extended to a 3-D configuration in subsec. 4.3.

The codes HELENA [2] and VMEC [21] yield the equilibrium configuration, where HELENA is axisymmetric and VMEC is 3-D. For stability comparison, MISHKA [2] is used, which is a general-n code that employs axisymmetric HELENA equilibria, as well as COBRA [3], which is an infinity-n stability code that makes use of an Eikonal formulation and investigates the stability of 3-D VMEC equilibria by solving the Ballooning equation. The numerical tool ELITE [4], referenced to in the introduction, is not compared with directly, but ELITE has been verified extensively with MISHKA itself.

Note that all stability results concern the most unstable mode and are stated using MISHKA normalization, using the major radius at the magnetic axis and the toroidal magnetic field on axis.

4.1. CBM18 Equilibrium Model

The axisymmetric circular tokamak model called CBM18 is used, which is designed to be ballooning unstable[6] through a steep pressure gradient [22]. This model is used in HELENA format as well as ported to the VMEC format. Fig. 2a shows pressure p and safety factor q, that are flux quantities, with dependence only on ψ. A poloidal cross-section of this circular tokamak model is shown as well in fig. 2b.

[6] Careful verification using peeling cases has to wait for a correct implementation of the vacuum term $\boldsymbol{\xi}^{\text{vac}}$ subsction 3.1.

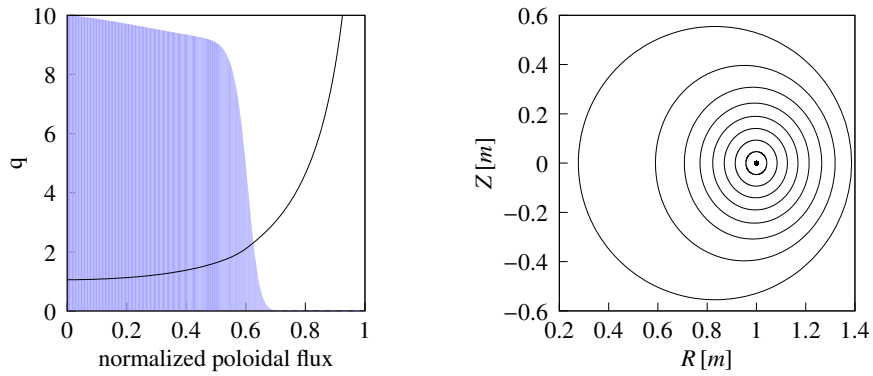

(a) The flux quantities safety factor q (solid line) and the pressure p (shaded, normalized to value at magnetic axis).

(b) Shifted-circle circular cross-section, showing magnetic axis, plasma edge, and seven equidistant internal flux surfaces.

Figure 2: Safety factor, pressure profile and cross-section for CBM18.

4.2. Axisymmetric verification

The PB3D results for CBM18 are directly compared to the results given by the numerical code MISHKA. In these simulations, the fast version of PB3D is used with 500 normal grid points, since increasing it beyond that number only marginally changes the results. In the Richardson extrapolation loop, the number of parallel grid points is automatically increased in the fundamental interval $-\pi \dots \pi$ until a relative error of 10^{-10} is reached. The number of poloidal harmonics, on the other hand, is manually increased until convergence of the most unstable eigenvalue was reached. In this axisymmetric case, the field line label α has no influence. Furthermore, COBRA [3] is also used to give the limit of $n \to \infty$. The results are plot in fig. 3.

There is good agreement with simulations done with the numerical codes ELITE and GATO in [22, fig. 6], taking into account a factor 1.5 due to the difference in normalization for the growth rate, due to the usage of $\frac{R}{B} = 1.5\frac{\mathrm{m}}{\mathrm{T}}$ instead of $1.0\frac{\mathrm{m}}{\mathrm{T}}$. Furthermore, there is similar behavior of increasing instability for higher n in both cases, i.e. for more localized modes. This is a consequence of the ability of the mode to become better and better localized in the regions of bad curvature. Also, it can be seen that they have the same marginal point, i.e. the mode number n for which there is marginal

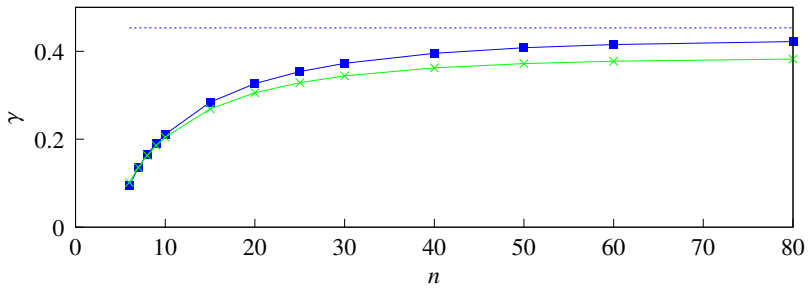

Figure 3: Comparison between results from PB3D (squares), MISHKA (crosses) and COBRA (dashed line). At every value for the primary mode number n, the number of secondary modes m is adjusted until convergence is reached, where the fast version of PB3D automatically sets the optimal resonating range.

stability. However, PB3D gives slightly more unstable results, but this is explained by the fact that the problems solved are basically of different nature between the two codes, due to the high-n approximation employed in the former code as compared to the general-n approach in the latter, which affects the different terms in a different way. In fact, the exact same phenomenon can be observed for ELITE, for example in [4, fig. 4], with a relative difference similar to the 10% obtained here. Furthermore, COBRA uses the infinite-n assumption, which makes it represent the limiting case, as can be seen from the figure.

Subsequently, fig. 4 shows a comparison of the mode structure between PB3D and MISHKA simulations for a CBM18 run with $n = 10$, using 30 Fourier modes with optimally chosen m. In fig. 4a, it can be seen that the individual Fourier mode amplitudes $X_m(\psi)$ as well as the global envelope show a Maxwellian structure around the pressure drop, as expected from infinity-n theory [7]. Furthermore, the destabilizing ballooning effect is obtained through the normal displacement of the individual modes with mode numbers m, each resonating on its own rational surface $q \approx \frac{m}{n}$ (not shown). In figs. 4b and 4c, a visual comparison is displayed between PB3D and MISHKA of the global mode structure of $X(\psi, \theta)$ in a poloidal cross-section.

Finally, the energy reconstruction discussed in the paragraph concerning the post-processing driver, is employed as a check on physical consistency: In fig. 5, a comparison is made between the calculated eigenvalue λ and the ratio of potential to kinetic

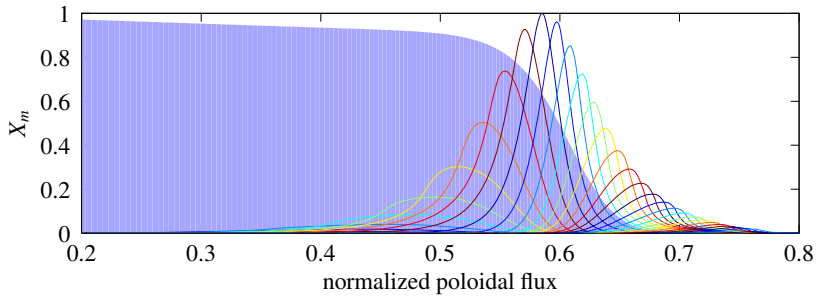

(a) Modes X_m at midplane and pressure p (shaded, normalized to value at magnetic axis)

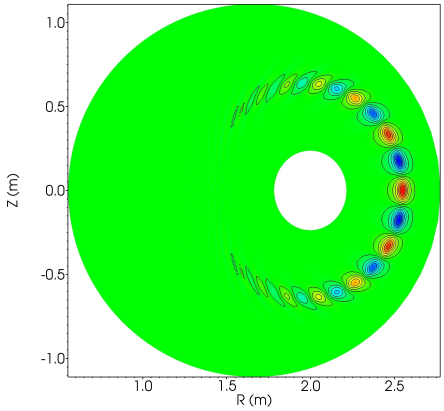

(b) Global mode structure in poloidal cut $\zeta = 0$ for PB3D.

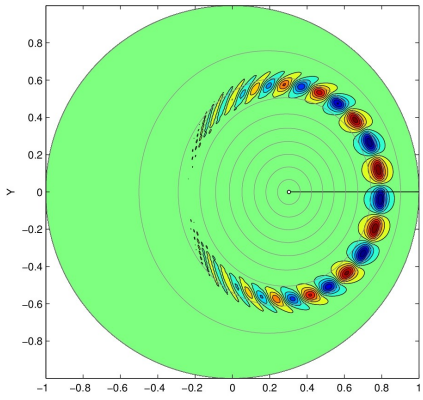

(c) And for MISHKA. (G. Huijsmans)

Figure 4: Most unstable mode for a simulation of the stability of CBM18 using $n = 10$ and 30 modes m.

energies in the Rayleigh Quotient Λ through energy reconstruction for different numbers of normal grid points (fig. 5a) and in the discretization of the eigenvector (fig. 5b). It can be seen that the energy reconstruction improves for increasing number of equilibrium grid points, but that the improvement for increasing the grid points of the discretization of the eigenvector only works up to the same order as the number of grid points in the underlying equilibrium model.

4.3. 3-D verification

The VMEC version of CBM18 has been adapted to a 3-D version through varying the poloidal cross-section radius $a(\zeta)$ toroidally by 10% over the whole toroidal range

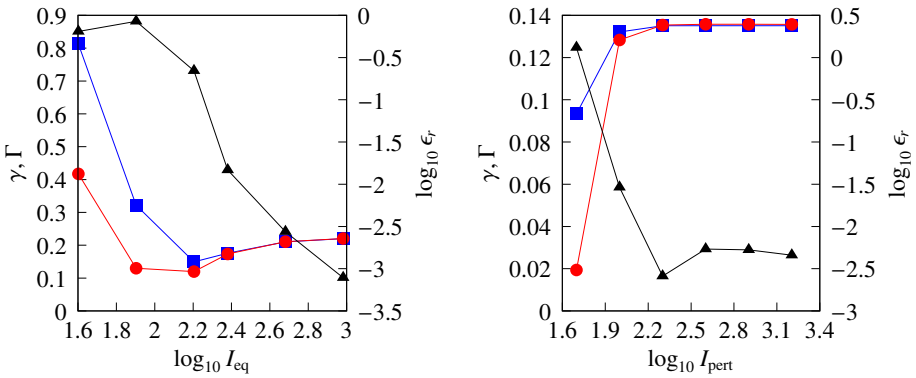

(a) Varying points I_{eq} in VMEC equilibrium.

(b) Varying points I_{pert} in discretization.

Figure 5: Energy reconstruction as a function of the number of grid points in the VMEC equilibrium model and in the discretization of the eigenvector. The number of grid points of either the discretization of the eigenvector or the VMEC equilibrium that is not varied, is kept constant at 500, and the simulations were done using $n = 10$, with 20 modes m. At left axis, squares show $\gamma = \sqrt{-\lambda}$ and circles show reconstructed $\Gamma = \sqrt{-\Lambda}$. At right axis, triangles show the relative difference ϵ_{rel} in logarithmic scale.

$\zeta = 0 \ldots 2\pi$, meaning that $\frac{\alpha(0)}{\alpha(\pi)} = 1.1$. The pressure profile and safety factor is unchanged and the position of the magnetic axis approximately so. Admittedly artificial, what matters is that this test case is 3-D.

This is reflected in a change of most unstable growth rate,[7] which is seen in fig. 6, showing the results from PB3D and COBRA, as well as the results copied from the axisymmetric case, which is refered to as the *large* case.

Also, a *small* case is provided, which corresponds to the axisymmetric configuration with a cross section equal to the smaller end of the modified 3-D case with constant radius equal to a (π) of the 3-D case. This small case was designed to have the same pressure profile as the large case, and the same safety factor. It is not directly evident why the small case is slightly more unstable in the limit $n \to \infty$ but with the marginal n-value

[7] It should be mentioned that other types of toroidal modifications, such as by squishing and expanding just the height or major radius, or applying a twist, have been tested and confirmed to generally lead to qualitative similar results. The same counts for toroidal modifications with more periods. The physical investigations of these configurations will be a subject of further work.

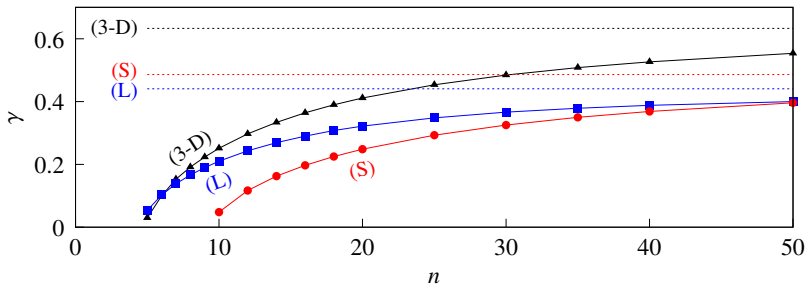

Figure 6: Comparison between 3-D results from PB3D (triangles) and COBRA (dashed line), as well as the original large (L) axisymmetric results (PB3D with squares and COBRA with dashed line from figure 6), and results for the smaller (S) axisymmetric version (PB3D with circles and COBRA with dashed line). Again, the primary mode n is varied and for every value of it, the number of secondary modes m is adjusted until convergence is reached, where the fast version of PB3D automatically sets the most resonating range. The 3-D result is more unstable than either the small or big CBM18 axisymmetric result.

higher than the large case, but in figure 7 the energy reconstruction is provided. In this figure, the relative contributions of six components of the plasma potential energy are plot, corresponding to the normal and geodesic components of the line-bending energy which is always stabilizing; the ballooning term (proportional to the pressure gradient) and the peeling term (proportional to the parallel current), which can be destabilizing. (See for example [17, eq. 8.87].) It can be seen that the difference between the large and small case is indeed quantitative.

Now, curiously, it can be seen that the PB3D results for the 3-D equilibrium are more unstable than either the small and large cases, an effect also observed in COBRA. To investigate this, the energy reconstruction is also displayed in figure 7. The main difference now is the large destabilizing normal component of the ballooning term, and the reduced compensation by stabilizing line bending. And though the geodesic components of both the ballooning and kink term are even slightly stabilizing, perhaps contrary to expectations, due to the toroidal change that has been created by merging the two axisymmetric cases, this is a far smaller effect.

Admittedly, it is an artificial test case, but clearly 3-D results can in some cases deviate strongly from axisymmetric ones PB3D provides the tool to study this.

Finally, contrary to the axisymmetric case, for these 3-D configurations, a discussion

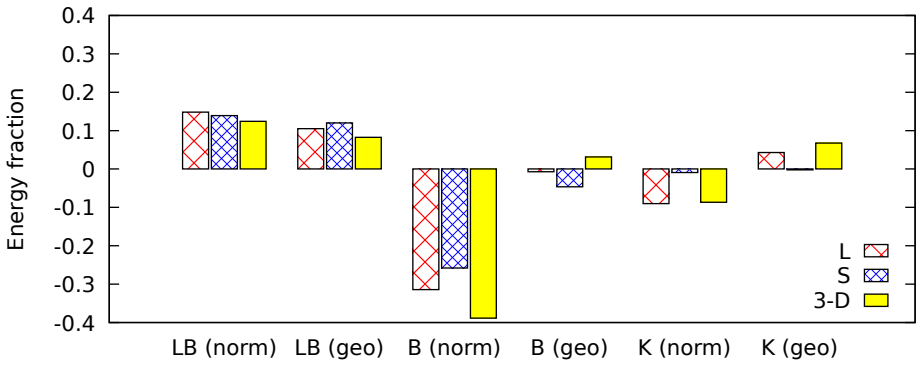

Figure 7: Comparison of potential energy terms for $n = 20$. These consist of the stabilizing line bending energy (LB) and the potentially destabilizing ballooning term (B) and kink term (K), displaying the normal components and geodesic components individually. This is done for the large (L) and small (S) axisymmetric cases, and the hybrid 3-D case, described above.

regarding the influence of the field-line label α and the limits $\theta_{\max}$ on the parallel bounding box $-\theta_{\max} \leq \theta \leq \theta_{\max}$ is important, which will also provide a check on physical consistency: Namely, α can be understood as the base of the magnetic field lines, i.e. the toroidal position ζ_0 at the midplane $\theta = 0$. As the entire flux surface is covered by the field lines, along which is integrated in the magnetic average modes (eq. 13), the parallel integration should range from $-\infty \ldots \infty$. It should therefore be expected that the field line label α have no influence on the final results.

Fig. 8a shows how well this is approximated in practice using a parallel bounding box of finite size. It can clearly be seen that the results for small bounding boxes are strongly dependent on α, which reflects that the modes are artificially confined to only use the information of a limited subspace of the 2-D flux surfaces. For larger sizes of bounding boxes—and correspondingly larger number of parallel points—the difference, however, falls of linearly with the size as can be seen in fig. 8b.

5. Summary

The new 3-D linear ideal high-n MHD stability code PB3D is presented, which simulates the high-n ideal linear MHD stability in 3-D magnetic configurations including

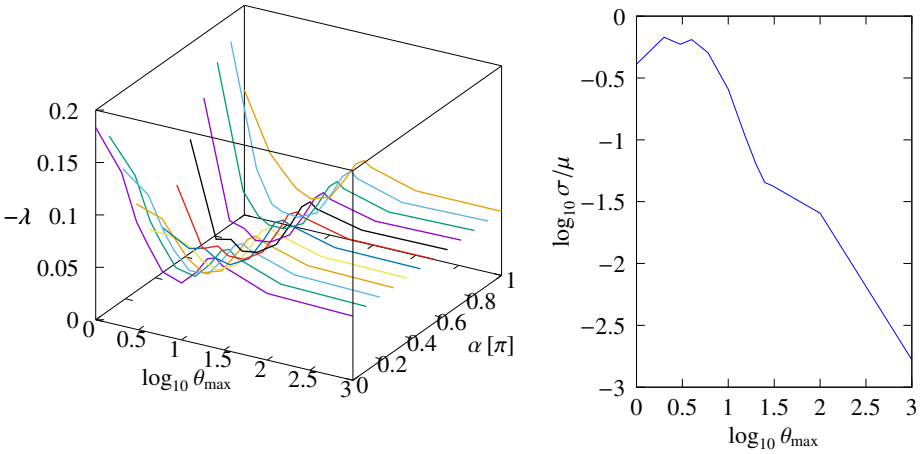

(a) eigenvalues for different field line labels α and different bouding box sizes $\theta_{\max}$, showing convergence for large box sizes.

(b) Evolution of the standard deviation σ divided by the average μ, as a function of the box size $\theta_{\max}$.

Figure 8: The influence of the bounding box in the parallel direction $\theta_{\max}$.

edge effects. Typical high-n modes that appear are peeling-ballooning modes, which have been linked to, for example, ELM cycling phenomena observed, as well as RMP techniques that break the axisymmetry of plasma for controlling them. It is expected that 3-D configurations offer can offer exciting new insights, such as possible new ranges in parameter space of enhanced stability. Furthermore, it is important that edge effects are taking into account correctly.

This paper focused on verifying the PB3D code using checks on physical consistency as well as by comparing results with MISHKA and COBRA. Good qualitative agreement is found and the quantitative differences are explained through differences in assumptions between these numerical codes. Furthermore, since MISHKA and COBRA have each been extensively benchmarked with other codes (such as ELITE, GATO for MISHKA, or TERPSICHORE for COBRA), this verification exercise has provided further confirmation of the correctness of the approach used in PB3D and its implementation. A first proof of the capabilities of the code is also presented with some non-intuitive results considering 3-D effects, with the aim of providing a numerical tool

that can be used to study them. Further work will focus on the applications of the code and extracting physical results.

Acknowledgements

ITER is the Nuclear Facility INB no. 174. The views and opinions expressed herein do not necessarily reflect those of the ITER Organization

This research was sponsored in part by DGICYT (Dirección General de Investigaciones Científicas y Tecnológicas) of Spain under Project No. ENE2015-68265

References

[1] T. Weyens, R. Sánchez, L. García, A. Loarte, G. T. A. Huysmans, Three-dimensional linear peeling-ballooning theory in magnetic fusion devices, Physics of Plasmas 21 (4) (2014) 042507. doi:10.1063/1.4871859.
URL http://dx.doi.org/10.1063/1.4871859

[2] A. B. Mikhailovskii, G. T. A. Huysmans, W. O. K. Kerner, S. E. Sharapov, Optimization of computational MHD normal-mode analysis for tokamaks, Plasma Physics Reports 23 (10) (1997) 844–857.

[3] R. Sánchez, S. P. Hirshman, J. C. Whitson, A. S. Ware, Cobra: An optimized code for fast analysis of ideal ballooning stability of three-dimensional magnetic equilibria, Journal of Computational Physics 161 (2) (2000) 576–588. doi:10.1006/jcph.2000.6514.
URL http://dx.doi.org/10.1006/jcph.2000.6514

[4] H. R. Wilson, P. B. Snyder, G. T. A. Huysmans, R. L. Miller, Numerical studies of edge localized instabilities in tokamaks, Physics of Plasmas 9 (4) (2002) 1277. doi:10.1063/1.1459058.
URL http://dx.doi.org/10.1063/1.1459058

[5] A. Loarte, G. T. A. Huijsmans, S. Futatani, L. R. Baylor, T. E. Evans, D. M. Orlov, O. Schmitz, M. Becoulet, P. Cahyna, A. Gribov, Y.and Kavin, A. Sashala

Naik, D. J. Campbell, T. Casper, E. Daly, H. Frerichs, A. Kischner, R. Laengner, S. Lisgo, R. A. Pitts, G. Saibene, A. Wingen, Progress on the application of ELM control schemes to ITER scenarios from the non-active phase to DT operation, Nucl. Fusion 54 (3) (2014) 033007. doi:10.1088/0029-5515/54/3/033007.
URL http://dx.doi.org/10.1088/0029-5515/54/3/033007

[6] J. M. Greene, J. L. Johnson, Interchange instabilities in ideal hydromagnetic theory, Plasma Physics 10 (8) (1968) 729–745. doi:10.1088/0032-1028/10/8/301.
URL http://dx.doi.org/10.1088/0032-1028/10/8/301

[7] J. W. Connor, R. J. Hastie, J. B. Taylor, High mode number stability of an axisymmetric toroidal plasma, Proceedings of the Royal Society A 365 (1720) (1979) 1–17. doi:10.1098/rspa.1979.0001.
URL http://dx.doi.org/10.1098/rspa.1979.0001

[8] J. W. Connor, R. J. Hastie, H. R. Wilson, R. L. Miller, Magnetohydrodynamic stability of tokamak edge plasmas, Physics of Plasmas 5 (7) (1998) 2687. doi:10.1063/1.872956.
URL http://dx.doi.org/10.1063/1.872956

[9] R. L. Dewar, A. H. Glasser, Ballooning mode spectrum in general toroidal systems, Physics of Fluids 26 (10) (1983) 3038–3052.

[10] R. D. Hazeltine, J. D. Meiss, Plasma Confinement, Dover books on physics, DOVER PUBN Incorporated, 2003.
URL http://books.google.co.uk/books?id=s3LQU_04GccC

[11] A. H. Boozer, Physics of magnetically confined plasmas, Rev. Mod. Phys. 76 (2005) 1071–1141. doi:10.1103/RevModPhys.76.1071.
URL http://link.aps.org/doi/10.1103/RevModPhys.76.1071

[12] J. P. Goedbloed, S. Poedts, Principles of Magnetohydrodynamics: With Applications to Laboratory and Astrophysical Plasmas, Cambridge University Press, 2004.
URL http://books.google.es/books?id=FvM6rMJob-cC

[13] I. T. Chapman, A. Kirk, C. J. Ham, J. R. Harrison, Y. Q. Liu, S. Saarelma, R. Scannell, A. J. Thornton, M. Becoulet, F. Orain, et al., Towards understanding edge localised mode mitigation by resonant magnetic perturbations in masta), Physics of Plasmas (1994-present) 20 (5) (2013) 056101.

[14] P. Helander, S. L. Newton, Ideal magnetohydrodynamic stability of configurations without nested flux surfaces, Physics of Plasmas (1994-present) 20 (6) (2013) 062504.

[15] C. C. Hegna, Effects of a weakly 3-d equilibrium on ideal magnetohydrodynamic instabilities, Physics of Plasmas (1994-present) 21 (7) (2014) 072502.

[16] C. Nührenberg, Global ideal magnetohydrodynamic stability analysis for the configurational space of wendelstein 7–x, Physics of Plasmas (1994-present) 3 (6) (1996) 2401–2410.

[17] J. P. Freidberg, Ideal magnetohydrodynamics, Modern perspectives in energy, Plenum Press, 1987.
URL http://books.google.es/books?id=UMDvAAAAMAAJ

[18] W. H. Press, Numerical recipes 3rd edition: The art of scientific computing, Cambridge university press, 2007.

[19] Z. Zhang, An improvement to the brent's method, International Journal of Experimental Algorithms 2 (1) (2011) 21–26.

[20] G. Dahlquist, Å. Björck, Numerical Methods, Dover Books on Mathematics, Dover Publications, 2003.
URL http://books.google.es/books?id=armfeHpJIwAC

[21] S. P. Hirshman, Steepest-descent moment method for three-dimensional magnetohydrodynamic equilibria, Phys. Fluids 26 (12) (1983) 3553. doi:10.1063/1.864116.
URL http://dx.doi.org/10.1063/1.864116

[22] N. M. Ferraro, S. C. Jardin, P. B. Snyder, Ideal and resistive edge stability calculations with m3d-c1, Physics of Plasmas 17 (10). doi:http://dx.doi.org/10.1063/1.3492727.
URL http://scitation.aip.org/content/aip/journal/pop/17/10/10.1063/1.3492727